

Measurements and Characteristics Analysis of 6G Ultra-Massive MIMO Wireless Channels With Different Antenna Configurations and Scenarios

Yi Zheng, Cheng-Xiang Wang [✉], *Fellow, IEEE*, Jie Huang [✉], *Member, IEEE*, Rui Feng [✉], *Member, IEEE*, and John Thompson [✉], *Fellow, IEEE*

Abstract—In this paper, ultra-massive multiple-input multiple-output (MIMO) channel measurements at 5.3 GHz are conducted, including different antenna array configurations and different measurement scenarios. The antenna array configurations include uniform linear array (ULA) and distributed uniform linear array (DULA). The measurement scenarios include single-user fixed-to-fixed (F2F), multi-user F2F, and single-user fixed-to-mobile (F2M) measurement scenarios. The statistical properties of ultra-massive MIMO channels are studied, including delay power spectral density (DPSD), space cross-correlation function (SCCF), angle cross-correlation function (ACCF), frequency correlation function (FCF), root mean square (RMS) delay spread (DS), RMS angle spread (AS), singular value spread (SVS), scalar product (SP), level crossing rate (LCR), average fading duration (AFD), Doppler power spectral density (PSD), etc. The specific ultra-massive MIMO channel characteristics are investigated and validated by channel measurements, including spatial non-stationarity, spherical wavefront behavior, channel hardening, and sparse properties in the angle domain. In addition, channel capacities are investigated. The channel measurement results will be a great importance for ultra-massive MIMO communication system deployments.

Index Terms—Ultra-massive MIMO, channel measurements, non-stationarity, sparse property, channel capacity.

Manuscript received 14 July 2022; revised 7 January 2023; accepted 15 February 2023. Date of publication 17 March 2023; date of current version 15 August 2023. This work was supported in part by the National Key R&D Program of China under Grant 2018YFB1801101, in part by the National Natural Science Foundation of China (NSFC) under Grants 61960206006 and 62271147, in part by the Key Technologies R&D Program of Jiangsu (Prospective and Key Technologies for Industry) under Grants BE2022067 and BE2022067-1, in part by the EU H2020 RISE TESTBED2 Project under Grant 872172, in part by the High Level Innovation and Entrepreneurial Doctor Introduction Program in Jiangsu under Grant JSSCBS20210082, and in part by the Fundamental Research Funds for the Central Universities under Grant 2242022R10067. The review of this article was coordinated by Prof. Sinem Coleri. (*Corresponding author: Cheng-Xiang Wang.*)

Yi Zheng, Cheng-Xiang Wang, and Jie Huang are with the National Mobile Communications Research Laboratory, School of Information Science and Engineering, Southeast University, Nanjing 210096, China, and also with the Purple Mountain Laboratories, Nanjing 211111, China (e-mail: zheng_yi@seu.edu.cn; chxwang@seu.edu.cn; j_huang@seu.edu.cn).

Rui Feng is with the Purple Mountain Laboratories, Nanjing 211111, China, and also with the School of Information Science and Engineering, Southeast University, Nanjing 210096, China (e-mail: fengxiurui604@163.com).

John Thompson is with the Institute for Digital Communications, School of Engineering, University of Edinburgh EH9 3JL Edinburgh, U.K. (e-mail: john.thompson@ed.ac.uk).

Digital Object Identifier 10.1109/TVT.2023.3258456

I. INTRODUCTION

THE development and evolution of the fifth generation (5G) communication systems promote various technologies. Compared with 5G communication systems, the sixth generation (6G) communication systems are expected to further improve the capacity. As an efficient way to enhance spectral efficiency, power efficiency, and spatial reuse, ultra-massive multiple-input multiple-output (MIMO) technology has attracted more and more attention for 6G communication systems [1], [2], [3], [4], [5]. Ultra-massive MIMO channel is the basis for the ultra-massive MIMO communication system design, performance evaluation, and optimization. With hundreds or even thousands of antennas employed in ultra-massive MIMO communication systems [6], [7], the ultra-massive MIMO channels have unique channel characteristics, such as spherical wavefront behavior, spatial non-stationarity, channel hardening, etc.

The channel characteristics of ultra-massive MIMO need to be further explored by channel measurements. At present, it is in the evolution stage from massive MIMO of 5G communication systems to ultra-massive MIMO of 6G communication systems. The number of antennas and the dimension of the array become larger and larger. There are a variety of massive MIMO channel measurements in the literature.

In [8], [9], outdoor stadium channel measurements were conducted at 1.4725 GHz with a 91 MHz bandwidth. A 128-port virtual uniform linear array (ULA) and a uniform cylindrical array (UCA) were employed at the base station (BS) side. The angle of departure (AoD) drifting along the ULA verified spherical wavefront behavior [10], [11], [12], [13]. In [14], [15], [16], [17], channel measurements were conducted at 2.6 GHz with a 50 MHz bandwidth. Similarly, a 128-port virtual ULA and a 128-port UCA or only a 128-port virtual ULA were employed at the BS side. By analyzing the Rician K-factor (KF) and received power levels changing along antenna array, spatial non-stationarity can be verified [12], [18]. In [19], outdoor urban channel measurements were conducted at 3.5 GHz with a bandwidth of 200 MHz and a 256-element virtual antenna array was employed at the BS side. Given the smaller channel capacities of the measurement channel compared to the independent identically distributed channel, it can be concluded that the favorable propagation condition can not

be realized. Note that the favorable propagation condition refers to the orthogonality of channel vectors for different users [20], [21].

In [22], outdoor urban channel measurements were conducted at 2.53 GHz with a 20 MHz bandwidth. The antenna arrays were a virtual UCA of 16×60 antennas at the transmitter (Tx) and a dual polarized 64-port uniform circular patch array at the receiver (Rx). The intra-cluster properties, inter-cluster properties, and correlation of cluster parameters were investigated. In [23], outdoor to indoor, urban microcell, and urban macrocell channel measurements were conducted at both 3.5 GHz and 6 GHz with 200 MHz bandwidths. Note that a uniform planar array (UPA) of 32 antennas was shifted in horizontal and vertical dimensions to form a virtual UPA of 256 antennas at the Tx. The Rx was equipped with 16 antennas. The multi-user channel capacity was investigated and was shown to improve with the increase of Tx antennas.

All the above massive MIMO channel measurements used virtual antenna arrays. In the literature, only a few massive MIMO channel measurements used physically large antenna arrays instead of virtual antenna arrays. In [24] and [25], channel measurements were conducted at 5.8 GHz with a bandwidth of 100 MHz. A 5.78 m long array of 128 monopole elements was employed at the BS side. The standard deviation of the mean power of the antenna array decreased when the number of antennas increased, which verified the channel hardening property [26]. In [26], ultra-massive MIMO channel measurements were conducted at 5.3 GHz with a 160 MHz bandwidth, including single-user and multi-user channel measurements. The delay power spectral density (PSD), angular PSD, space cross-correlation function (SCCF), normalized user-side correlation matrix, singular value spread (SVS), degrees of freedom (DoF), and diversity level were studied. However, ultra-massive MIMO channel measurements using physically large antenna arrays with different antenna configurations have not been sufficiently investigated. Comprehensive statistical properties of ultra-massive MIMO channels need to be further explored. In order to fill the gaps mentioned above, we conduct the ultra-massive MIMO channel measurements with different antenna configurations and in different measurement scenarios. The main contributions and novelties of this paper can be summarized as follows.

- 1) Ultra-massive MIMO channel measurements are conducted, including two antenna array configurations and three measurement scenarios. The two antenna array configurations include ULA and distributed uniform linear array (DULA). The three measurement scenarios include single-user fixed-to-fixed (F2F), multi-user F2F, and single-user fixed-to-mobile (F2M) measurement scenarios.
- 2) Comprehensive statistical properties are studied, such as delay power spectral density (DPSD), SCCF, angle cross-correlation function (ACCF), frequency correlation function (FCF), root mean square (RMS) delay spread (DS), RMS angle spread (AS), SVS, scalar product (SP), level crossing rate (LCR), average fading duration (AFD), Doppler PSD, etc.

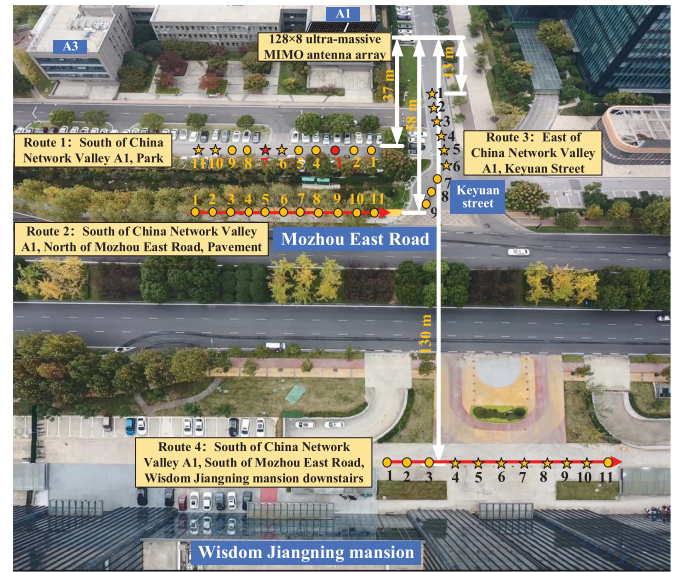


Fig. 1. The ultra-massive MIMO channel measurement scenarios.

- 3) Specific characteristics of massive MIMO channels are investigated and validated by channel measurements, including spatial non-stationarity, spherical wavefront behavior, channel hardening, and sparse properties in the angle domain.
- 4) Channel capacities are studied, including multi-user multiple access channel (MAC) capacity, multi-user interference channel (IC) capacity, and single-user channel capacity.

The rest of this paper is organized as follows. Section II introduces the ultra-massive MIMO channel measurements and data processing. Section III shows statistical properties and channel capacities. Section IV shows channel measurement results and analysis. Finally, conclusions are drawn in Section V.

II. ULTRA-MASSIVE MIMO CHANNEL MEASUREMENTS

The measurements are conducted at 5.3 GHz with a 160 MHz bandwidth using an ultra-massive MIMO channel sounder. The measurement scenarios include single-user F2F, multi-user F2F, and single-user F2M measurement scenarios. As shown in Fig. 1, 4 measurement routes are used. In addition, line-of-sight (LOS) positions are marked as stars and non-line-of-sight (NLOS) positions are marked as circles.

A. Ultra-Massive MIMO Channel Sounder

The equipment of the channel sounder at the Tx side includes a vector signal generator (VSG), a power amplifier (PA), a switch matrix, Tx antennas, and a GPS Rubidium clock. The equipment of the channel sounder at Rx side includes the 128×8 ultra-massive MIMO antenna array, switch matrices and controller, a low noise amplifier (LNA), a high speed disk array, and a GPS Rubidium clock. To study the impact of array aperture size on channel characteristics, we utilized two configurations of ultra-massive MIMO antenna arrays, i.e., ULA and DULA configurations as shown in Fig. 2.



Fig. 2. The configurations of the 128×8 ultra-massive MIMO antenna array.

1) *ULA Configuration*: The ULA configuration refers to the 128×8 ultra-massive MIMO antenna array being uniformly arranged with the spacing of 0.6 wavelength between the adjacent antennas in the horizontal dimension. The 8 antennas in the vertical dimension sharing one radio frequency (RF) channel are used for beamforming. Correspondingly, the beamwidths in the horizontal and vertical dimensions are $85^\circ \pm 4^\circ$ and $12^\circ \pm 2^\circ$, respectively. The overall size of the ULA is $4.3 \text{ m} \times 0.36 \text{ m}$.

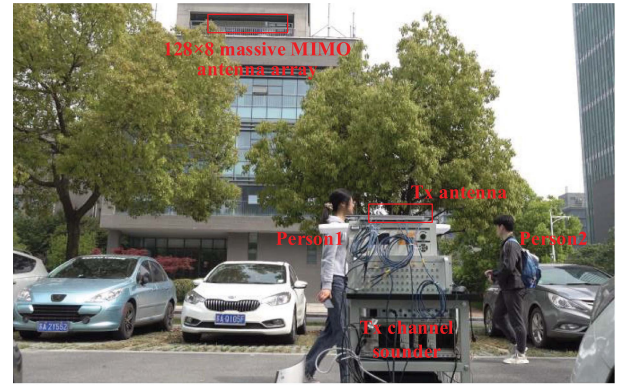
2) *DULA Configuration*: The DULA configuration refers to that the 128×8 ultra-massive MIMO antenna array is divided into distributed 8 subarrays. The spacing of adjacent subarrays is 0.4 m and the spacing between the adjacent antennas in subarray is 0.6 wavelength in the horizontal dimension. Thus, the overall size of the DULA is $7.2 \text{ m} \times 0.36 \text{ m}$.

B. Ultra-Massive MIMO Single-User F2F Measurements

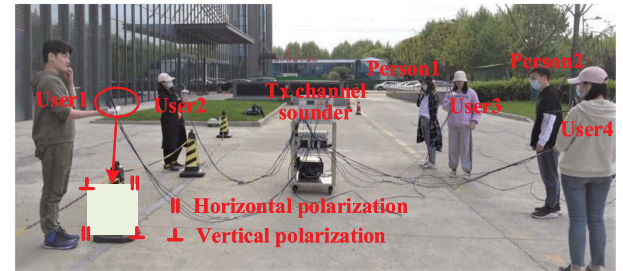
As shown in Fig. 1, the Tx is located on a truck in the positions marked as stars and circles with the antenna height about 1.5 m high. The Rx is located on the roof of a 20 m high A1 building marked as 128×8 ultra-massive MIMO antenna array. Ultra-massive MIMO single-user F2F measurements refer to the case that the Tx is a single user, which comprises 8 omnidirectional antennas in a line with horizontally and vertically polarized antennas arranged alternately. Note that the spacing between two adjacent antennas is 5 cm. The Rx is the 128×8 ultra-massive MIMO antenna array, which has two configurations including both ULA and DULA configurations. During the measurement campaigns, two persons move randomly around the Tx simulating user side interference. The ultra-massive MIMO single-user F2F measurement scenario is shown in Fig. 3(a).

C. Ultra-Massive MIMO Multi-User F2F Measurements

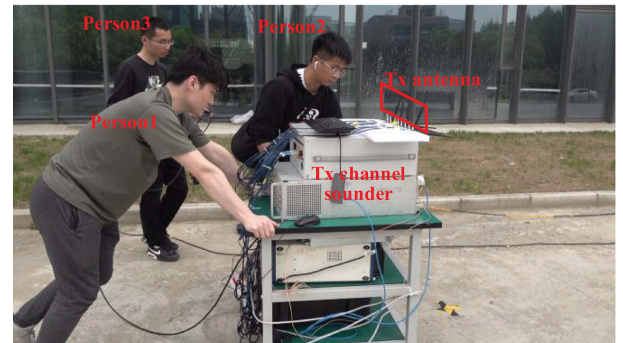
In this scenario, the Tx sounder is located on a truck in the positions marked as stars and circles as shown in Fig. 1 and the 4 users are located at the vertex positions of the square with the antenna height about 1.5 m high. Again, the Rx is located on the roof of a 20 m high A1 building marked as 128×8 ultra-massive MIMO antenna array, which is shown in Fig. 1. Ultra-massive MIMO multi-user F2F measurements refer to the case of 4 transmitting users and each user employs 4 omnidirectional antennas arranged at the vertex positions of the square. The spacing between two adjacent antennas is 5 cm. The 4 omnidirectional antennas are horizontally polarized in one diagonal but vertically polarized in another diagonal. Similarly, the Rx is a 128×8 ultra-massive MIMO antenna array, which has two configurations including both ULA and DULA



(a)



(b)



(c)

Fig. 3. The ultra-massive MIMO (a) single-user F2F, (b) multi-user F2F, and (c) single-user F2M channel measurement scenarios.

configurations. Two persons move randomly around the Tx simulating user side interference during the measurement campaigns. The ultra-massive MIMO multi-user F2F measurement scenario is shown in Fig. 3(b).

D. Ultra-Massive MIMO Single-User F2M Measurements

Finally, ultra-massive MIMO single-user F2M measurements refers to a single user Tx located on a truck pushed by three persons along Route 2 and Route 4, which have been marked as red arrow lines in Fig. 1. The Rx is a 128×8 ultra-massive MIMO antenna array, which is in the DULA configuration. The ultra-massive MIMO single-user F2M measurement scenario is shown in Fig. 3(c).

The ultra-massive MIMO channel sounder cooperating with switch matrices can support multi-channel extension. For single-user F2F and F2M measurements, the Tx side consists of 8 channels in serial and the Rx side consists of 4 channels in parallel

with 32 channels in serial for each parallel channel. Totally, there are 128×8 channels in the single-user measurement scenario. Similarly, the Tx side consists of 16 channels in serial and the Rx side consists of 4 channels in parallel with 32 channels in serial for each parallel channel. Thus, there are totally 128×16 channels in the multi-user F2F measurement scenario.

The transmitting waveform used for channel measurements is a 6400 points pseudo noise (PN) sequence repeated by a 1023 points short PN. The 4 switch matrices at the Rx side have damaged channels and 4 channels for each switch matrix are added. Hence, the durations of one snapshot are 11.52 ms in the single-user measurement scenario and 23.04 ms in the multi-user measurement scenario. At the Rx side, the known 1023 points short PN is convolved with the received signal to obtain the one correlation peak in the middle. Note that the other five correlation peaks are discarded to avoid interference caused by switching. The above method is an effective way to obtain the desired channel impulse response (CIR). For each position of the single-user F2F measurement scenario, 434 snapshots are saved for 5 s. Similarly, 217 snapshots are saved for 5 s at each position of the multi-user F2F measurement scenario.

E. Channel Measurement Data Processing

1) *Acquisition of CIR*: To eliminate the response of measurement equipment, system calibration need to be carried out. Through corresponding data processing, the corresponding CIR can be obtained.

Let us assume that $x(t)$ is the transmitted signal, $y(t)$ is the received signal, $g(t)$ is the response of the measurement equipment, and $h(t)$ is the CIR. The direct calibration signal $y_{th}(t)$ can be expressed as

$$y_{th}(t) = x(t) * g(t) \quad (1)$$

where $*$ represents convolution in the time domain. Similarly, the received signal $y(t)$ can be calculated by channel measurement

$$y(t) = x(t) * g(t) * h(t). \quad (2)$$

The corresponding frequency domain channel transfer functions (CTFs) can be obtained by taking the Fourier transformations of (1) and (2)

$$Y_{th}(f) = X(f)G(f) \quad (3)$$

and

$$Y(f) = X(f)G(f)H(f). \quad (4)$$

Then, the CIR can be obtained by taking the inverse fast Fourier transform (IFFT) of $H(f)$

$$h(t) = IFFT(H(f)) = IFFT(Y(f)/Y_{th}(f)). \quad (5)$$

2) *Estimation of Channel Parameters*: The channel parameters of the l th multipath components (MPCs) are estimated, including complex amplitude α_l , delay τ_l , azimuth angle of departure (AAoD) $\phi_{T,l}$, azimuth angle of arrival (AAoA) $\phi_{R,l}$, elevation angle of departure (EAoD) $\theta_{T,l}$, elevation angle of arrival (EAoA) $\theta_{R,l}$, and Doppler frequency ν_l . Using the channel

parameters of MPCs, the received signal can be rewritten as

$$\begin{aligned} \mathbf{y}(t) = & \sum_{l=1}^L \alpha_l e^{j2\pi\nu_l t} c_R(\boldsymbol{\Omega}_{R,l}) c_T(\boldsymbol{\Omega}_{T,l})^T x(t - \tau_l) \\ & + \sqrt{\frac{N_0}{2}} \mathbf{N}(t). \end{aligned} \quad (6)$$

In (6), $\mathbf{N}(t)$ is the standard complex white Gaussian noise with PSD N_0 , $(\cdot)^T$ is the transpose operation, L is the number of MPCs, and the steering vector $c_T(\boldsymbol{\Omega}_{T,l})$ of the Tx array and the response vector $c_R(\boldsymbol{\Omega}_{R,l})$ of the Rx array [27] can be expressed as

$$\begin{aligned} c_T(\boldsymbol{\Omega}_{T,l}) = & \left[e^{j2\pi\lambda^{-1}\langle \boldsymbol{\Omega}_{T,l}, \mathbf{r}_{T,1} \rangle}, e^{j2\pi\lambda^{-1}\langle \boldsymbol{\Omega}_{T,l}, \mathbf{r}_{T,2} \rangle}, \right. \\ & \left. \dots, e^{j2\pi\lambda^{-1}\langle \boldsymbol{\Omega}_{T,l}, \mathbf{r}_{T,M_T} \rangle} \right]^T \end{aligned} \quad (7)$$

and

$$\begin{aligned} c_R(\boldsymbol{\Omega}_{R,l}) = & \left[e^{j2\pi\lambda^{-1}\langle \boldsymbol{\Omega}_{R,l}, \mathbf{r}_{R,1} \rangle}, e^{j2\pi\lambda^{-1}\langle \boldsymbol{\Omega}_{R,l}, \mathbf{r}_{R,2} \rangle}, \right. \\ & \left. \dots, e^{j2\pi\lambda^{-1}\langle \boldsymbol{\Omega}_{R,l}, \mathbf{r}_{R,M_R} \rangle} \right]^T. \end{aligned} \quad (8)$$

Here, $\langle \boldsymbol{\Omega}_{T,l}, \mathbf{r}_{T,p} \rangle$ and $\langle \boldsymbol{\Omega}_{R,l}, \mathbf{r}_{R,q} \rangle$ are the inner product operators corresponding to the p th ($p = 1, 2, \dots, M_T$) Tx antenna and the q th ($q = 1, 2, \dots, M_R$) Rx antenna, respectively, M_T and M_R are the numbers of Tx antennas and Rx antennas, respectively, and $\mathbf{r}_{T,p}$ and $\mathbf{r}_{R,q}$ are the position vectors of the p th Tx antenna and q th Rx antenna, respectively. The $\boldsymbol{\Omega}_{T,l}$ and $\boldsymbol{\Omega}_{R,l}$ are unit vectors can be further expressed as

$$\boldsymbol{\Omega}_{T,l} = [\sin(\theta_{T,l}) \sin(\phi_{T,l}), \sin(\theta_{T,l}) \cos(\phi_{T,l}), \cos(\theta_{T,l})]^T \quad (9)$$

and

$$\boldsymbol{\Omega}_{R,l} = [\sin(\theta_{R,l}) \sin(\phi_{R,l}), \sin(\theta_{R,l}) \cos(\phi_{R,l}), \cos(\theta_{R,l})]^T. \quad (10)$$

The space-alternating generalized expectation-maximization (SAGE) algorithm [28], [29], [30] can be used to extract the above-mentioned channel parameters.

III. STATISTICAL PROPERTIES AND CHANNEL CAPACITIES

Denote $\mathbf{H}_k(s, u) \in \mathbb{C}^{M_R \times M_T}$ as the discretized realization of uplink channel matrix $\mathbf{H}_k(t, f) \in \mathbb{C}^{M_R \times M_T}$ for the s th ($s = 1, 2, \dots, N_s$) snapshot, u th ($u = 1, 2, \dots, N_f$) frequency point, and k th ($k = 1, 2, \dots, K$) user. Here, N_s is the number of snapshots, N_f is the number of frequency points, and K is the number of users. The discretized realization of multi-user uplink channel matrix $\mathbf{H}_{\text{mul}}(t, f) \in \mathbb{C}^{M_R \times K M_T}$ for the s th snapshot and u th frequency point can be expressed as

$$\begin{aligned} \mathbf{H}_{\text{mul}}(s, u) \in & \mathbb{C}^{M_R \times K M_T} = \\ & [\mathbf{H}_1(s, u), \mathbf{H}_2(s, u), \dots, \mathbf{H}_K(s, u)]. \end{aligned} \quad (11)$$

Here, $K M_T$ represents the total number of Tx antennas for the multi-user uplink channel matrix. When $K = 1$, the multi-user

uplink channel matrix can be simplified to single-user uplink channel matrix $\mathbf{H}(t, f) \in \mathbb{C}^{M_R \times M_T}$. The q th row and p th column element of $\mathbf{H}(t, f)$ is expressed as $H_{qp}(t, f)$.

Correspondingly, the angle domain channel matrix in the far field can be expressed as [31], [32]

$$\mathbf{H}^b(t, f) = \mathbf{U}_R^H \mathbf{H}(t, f) \mathbf{U}_T. \quad (12)$$

In (12), $(\cdot)^H$ represents the conjugate transpose operator, $\mathbf{H}^b(t, f) \in \mathbb{C}^{M_R^b \times M_T^b}$, M_R^b and M_T^b are the numbers of beams at the Rx and Tx sides, respectively, and \mathbf{U}_R and \mathbf{U}_T are the unitary matrices defined as [32]. The q_b th ($q_b = 1, 2, \dots, M_R^b$) row and p_b th ($p_b = 1, 2, \dots, M_T^b$) column element of $\mathbf{H}^b(t, f)$ is expressed as $H_{q_b p_b}(t, f)$. Similarly, the discretized realization of the angle domain channel matrix for the s th snapshot and u th frequency point can be expressed as $\mathbf{H}^b(s, u)$.

A. Statistical Properties

1) *DPSD*: The DPSD describes the power distribution along the delay domain, which can be calculated as

$$\text{DPSD} = \sum_{l=1}^L P_l \delta(\tau - \tau_l). \quad (13)$$

In (13), P_l is the power of the l th MPCs which can be expressed as $P_l = |\alpha_l|^2$ and $\delta(\cdot)$ is the Delta function.

2) *SCCF and ACCF*: The SCCF describes the correlation of different antennas along antenna array, which can be expressed as

$$\begin{aligned} \gamma_{qp, q'p'}(t, f; \delta_T, \delta_R) &= E [H_{qp}(t, f) H_{q'p'}^*(t, f)] = \frac{K_{RF}}{K_{RF} + 1} \\ &\cdot \gamma_{qp, q'p'}^L(t, f; \delta_T, \delta_R) + \frac{1}{K_{RF} + 1} \cdot \gamma_{qp, q'p'}^N(t, f; \delta_T, \delta_R). \end{aligned} \quad (14)$$

In (14), $(\cdot)^*$ is the conjugate operator, $E[\cdot]$ is the expectation operator, K_{RF} is the KF, $\gamma_{qp, q'p'}^L(t, f; \delta_T, \delta_R)$ and $\gamma_{qp, q'p'}^N(t, f; \delta_T, \delta_R)$ are the SCCFs of LOS and NLOS parts, respectively, p and p' represent the different Tx antennas, q and q' represent the different Rx antennas, and δ_T and δ_R represent the distances between two adjacent antennas at the Tx and Rx sides, respectively.

The ACCF describes the correlation of different beams along the angle domain, which can be expressed as

$$\begin{aligned} \gamma_{q_b p_b, q'_b p'_b}(t, f; \delta_{T_b}, \delta_{R_b}) &= E [H_{q_b p_b}(t, f) H_{q'_b p'_b}^*(t, f)] = \\ &\frac{K_{RF}}{K_{RF} + 1} \cdot \gamma_{q_b p_b, q'_b p'_b}^L(t, f; \delta_{T_b}, \delta_{R_b}) + \frac{1}{K_{RF} + 1} \\ &\cdot \gamma_{q_b p_b, q'_b p'_b}^N(t, f; \delta_{T_b}, \delta_{R_b}). \end{aligned} \quad (15)$$

In (15), $\gamma_{q_b p_b, q'_b p'_b}^L(t, f; \delta_{T_b}, \delta_{R_b})$ and $\gamma_{q_b p_b, q'_b p'_b}^N(t, f; \delta_{T_b}, \delta_{R_b})$ are the ACCFs of LOS and NLOS parts, respectively, p_b and p'_b represent the different Tx beams, q_b and q'_b represent the different Rx beams, and δ_{T_b} and δ_{R_b} represent the angle differences between two adjacent beams at the Tx and Rx, respectively.

3) *FCF in the Array and Angle Domains*: The FCF describes the correlation of different frequencies and the FCF in the array domain can be denoted as

$$\begin{aligned} \varkappa_{qp, qp}(t, f; \Delta f) &= E [H_{qp}(t, f) H_{qp}^*(t, f + \Delta f)] = \\ &\frac{K_{RF}}{K_{RF} + 1} \varkappa_{qp, qp}^L(t, f; \Delta f) + \frac{1}{K_{RF} + 1} \varkappa_{qp, qp}^N(t, f; \Delta f). \end{aligned} \quad (16)$$

In (16), Δf is the frequency difference, $\varkappa_{qp, qp}^L(t, f; \Delta f)$ and $\varkappa_{qp, qp}^N(t, f; \Delta f)$ are the FCFs of LOS and NLOS parts in the array domain, respectively.

Similarly, the FCF in the angle domain can be denoted as

$$\begin{aligned} \varkappa_{q_b p_b, q_b p_b}(t, f; \Delta f) &= E [H_{q_b p_b}(t, f) H_{q_b p_b}^*(t, f + \Delta f)] = \\ &\frac{K_{RF}}{K_{RF} + 1} \varkappa_{q_b p_b, q_b p_b}^L(t, f; \Delta f) \\ &+ \frac{1}{K_{RF} + 1} \varkappa_{q_b p_b, q_b p_b}^N(t, f; \Delta f). \end{aligned} \quad (17)$$

In (17), $\varkappa_{q_b p_b, q_b p_b}^L(t, f; \Delta f)$ and $\varkappa_{q_b p_b, q_b p_b}^N(t, f; \Delta f)$ are the FCFs of LOS and NLOS parts in the angle domain, respectively.

4) *RMS DS and RMS AS*: RMS DS describes the powers of MPCs spread over the delay domain, which can be expressed as [33]

$$\text{DS} = \sqrt{\frac{\sum_{l=1}^L P_l \tau_l^2}{\sum_{l=1}^L P_l} - \left(\frac{\sum_{l=1}^L P_l \tau_l}{\sum_{l=1}^L P_l} \right)^2}. \quad (18)$$

The RMS AS of AAoA represents the powers of MPCs spread over the azimuth angle, which can be expressed as [34]

$$\text{AS} = \sqrt{\frac{\sum_{l=1}^L P_l \phi_{R,l}^2}{\sum_{l=1}^L P_l} - \left(\frac{\sum_{l=1}^L P_l \phi_{R,l}}{\sum_{l=1}^L P_l} \right)^2}. \quad (19)$$

5) *SVS*: The SVS is an indicator used to measure the correlation between different users and can be obtained by the singular value decomposition (SVD) of the channel matrix. Considering the downlink multi-user channel matrix $\mathbf{H}_{\text{mul}}^T$, the SVD can be expressed as

$$\mathbf{H}_{\text{mul}}^T = \mathbf{U} \mathbf{\Sigma} \mathbf{V}. \quad (20)$$

In (20), $\mathbf{\Sigma}$ is a $K M_T \times M_R$ diagonal matrix composed of singular values, \mathbf{U} and \mathbf{V} are unitary left and right matrices and the corresponding sizes are $K M_T \times K M_T$ and $M_R \times M_R$, respectively. In our channel measurements, $K M_T = 16$ is much smaller than $M_R = 128$. Hence, the number of the singular values is $K M_T$. Correspondingly, the SVS can be expressed as [26]

$$\kappa_{\text{svs}} = \frac{\max_j \sigma_j}{\min_j \sigma_j}. \quad (21)$$

Here, $\sigma_1, \sigma_2, \dots, \sigma_{K M_T}$ are the $K M_T$ singular values. Note that a larger SVS value indicates that at least two users' channel vectors are almost parallel, which means that the two users have a strong correlation.

6) *SP*: The SP is used to describe the correlation between two different users, which can be defined as

$$\text{SP} = \frac{1}{N_s} \sum_{s=1}^{N_s} \frac{|\mathbf{h}_1(s)' \mathbf{h}_2(s)|}{\|\mathbf{h}_1(s)\| \|\mathbf{h}_2(s)\|}. \quad (22)$$

In (22), $\|\cdot\|$ is Euclidean norm of the vector, and $\mathbf{h}_1(s)$ and $\mathbf{h}_2(s)$ are the channel vectors of antenna 1 of user 1 and antenna 1 of user 2 at 5.3 GHz frequency point for the s th snapshot. The size of these is $M_R \times 1$. It is worth mentioning that a larger SP represents a larger correlation between users.

7) *Normalized Channel Matrix in the Array and Angle Domains*: The normalized channel matrix in the array domain can be expressed as

$$\mathbf{H}_{\text{nor}}(u) = \frac{1}{N_s} \sum_{s=1}^{N_s} \mathbf{H}(s, u). \quad (23)$$

Similarly, the normalized channel matrix in the angle domain can be expressed as

$$\mathbf{H}_{\text{nor}}^b(u) = \frac{1}{N_s} \sum_{s=1}^{N_s} \mathbf{H}^b(s, u). \quad (24)$$

8) *Doppler PSD*: The Doppler shift is caused by the movement of the Tx. The Doppler PSD in the array domain can be defined as [35], [36], [37], [38]

$$\psi(t, \nu, f) = \int E[H_{qp}(t, f) H_{qp}^*(t + \Delta t, f)] e^{-j2\pi\nu\Delta t} d\Delta t \quad (25)$$

where Δt is the time difference.

Similarly, taking the Fourier transform of $E[H_{qbpb}(t, f) H_{qbpb}^*(t + \Delta t, f)]$ in the time domain, the Doppler PSD in the angle domain can be defined as [39]

$$\psi_b(t, \nu, f) = \int E[H_{qbpb}(t, f) H_{qbpb}^*(t + \Delta t, f)] e^{-j2\pi\nu\Delta t} d\Delta t. \quad (26)$$

B. Channel Capacities

1) Multi-User Channel Capacity:

a) *MAC Capacity*: Channel capacity is the maximum rate in the channel for which the bit error rate tends to zero. When the Tx is equipped with 4 users and the Rx is equipped with the ULA or DULA, the multi-user maximum MAC capacity can be calculated as [40]

$$C_{\text{mac}} = \frac{1}{N_s N_f} \sum_{s,u} \log_2 \left[\det \left(\mathbf{I}_{M_R} + \sum_{k=1}^K \frac{\rho_k}{M_T} \hat{\mathbf{H}}_k(s, u) \hat{\mathbf{H}}_k^H(s, u) \right) \right]. \quad (27)$$

In (27), $\det[\cdot]$ represents the determinant operator, ρ_k represents the signal-to-noise ratio (SNR) for the k th user, \mathbf{I}_{M_R} represents the identity matrix of order M_R , and $\hat{\mathbf{H}}_k$ is the normalized channel matrix for the k th user which can be calculated as $\hat{\mathbf{H}}_k(s, u) = \mathbf{H}_k(s, u) / \sqrt{P_r(s, u)}$. The normalized received

power can be calculated as $P_r(s, u) = \frac{1}{M_R M_T} \|\mathbf{H}_k(s, u)\|_F^2$. Here, $\|\cdot\|_F$ is the Frobenius norm of a matrix.

b) *IC Capacity*: The Rx is equipped with the ULA or DULA and the Tx is equipped with 4 users. The 4 users communicate with the ULA or DULA. The multi-user IC capacity can be calculated as [31], [40]

$$C_{\text{int}} = \sum_{k=1}^K \frac{1}{N_s N_f} \sum_{s,u} \log_2 \left[\det \left(\mathbf{I}_{M_R} + \left(\mathbf{I}_{M_R} + \sum_{i \neq k} \frac{\rho_i}{M_T} \hat{\mathbf{H}}_i(s, u) \hat{\mathbf{H}}_i^H(s, u) \right)^{-1} \frac{\rho_k}{M_T} \hat{\mathbf{H}}_k(s, u) \hat{\mathbf{H}}_k^H(s, u) \right) \right] \quad (28)$$

where ρ_i and $\hat{\mathbf{H}}_i$ represent the SNR and normalized channel matrix of the i th user, respectively.

2) *Single-User Channel Capacity*: When the Tx is equipped with a single user and the Rx is equipped with the ULA or DULA, the single-user ergodic channel capacity can be calculated as [26], [41]

$$C_{\text{sin}} = \frac{1}{N_s N_f} \sum_{s,u} \left[\log_2 \left[\det \left(\mathbf{I}_{M_R} + \frac{\rho}{M_T} \hat{\mathbf{H}}(s, u) \hat{\mathbf{H}}^H(s, u) \right) \right] \right]. \quad (29)$$

Here, ρ is the SNR and $\hat{\mathbf{H}}$ is the normalized single-user channel matrix. It can be calculated as $\hat{\mathbf{H}}(s, u) = \mathbf{H}(s, u) / \sqrt{P_r(s, u)}$. Here, $P_r(s, u) = \frac{1}{M_R M_T} \|\mathbf{H}(s, u)\|_F^2$.

IV. CHANNEL MEASUREMENTS RESULTS AND ANALYSIS

A. Single-User F2F Results and Analysis

1) *Non-Stationarity and Sparse Property*: Fig. 4(a) and (b) illustrate the measured and estimated DPDSs using a SAGE algorithm in LOS and NLOS environments, respectively. In the SAGE algorithm, 100 MPCs were selected by balancing the algorithm accuracy and complexity. We can see that most MPCs can be estimated except some weak MPCs with large delays. The big gap between estimation and measurement results for MPCs with weak powers and large delays is mainly due to the limitation of the SAGE algorithm. It is based on the order of power from large to small to extract MPCs and estimate their channel parameters. Note that the paths with weak powers and large delays have little influence on the SNR. Once the paths with strong powers and small delays are estimated, the channel characteristics can be analyzed accurately. The threshold levels in Fig. 4(a) and (b) are calculated by the larger one of noise base level plus 6 dB and maximum level minus 35 dB. The number of delay points marked as small pink stars above threshold level is the detected number of multipaths, which is calculated by peak search algorithm recommended in [42], [43]. Fig. 4(a) and (b) show that detected number of multipaths in NLOS environments is larger than that in LOS environments, which manifests that there are more scattering components in NLOS environments.

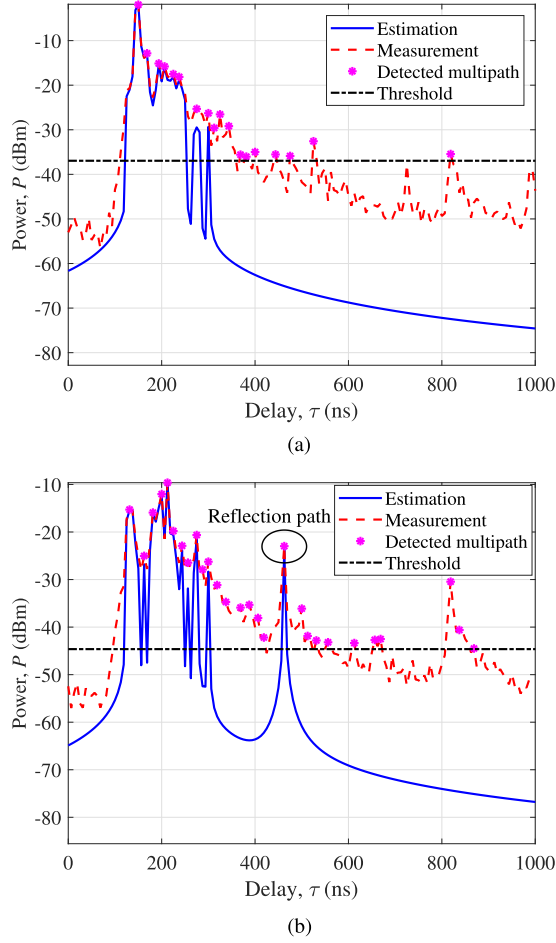


Fig. 4. The DPDSs in (a) LOS (Route 1, Position 7) and (b) NLOS (Route 1, Position 3) environments.

For clarity, we have marked a strong reflection path which has been detected by peak search algorithm in Fig. 4(b).

Fig. 5(a) and (b) illustrate the normalized channel matrices at 5.3 GHz frequency point for the array and angle domains in LOS environments, respectively. Fig. 5(c) and (d) illustrate the normalized channel matrices at 5.3 GHz frequency point for the array and angle domains in NLOS environments, respectively. The variations along the array and angle illustrate the non-stationarity in the array and angle domains. Note that the AAoA and AAoD are determined by the radiation patterns of antenna arrays at the Rx and Tx sides, respectively. Fig. 5(a) and (c) show that the energy is distributed along all the Rx antennas. Fig. 5(b) and (d) show that most of the energy is contained in a few AAoAs. Compared with Fig. 5(a) and (c) in the array domain, Fig. 5(b) and (d) in the angle domain show more obvious sparse property. Note that the sparse property refers to the fact that most of the channel coefficients in the normalized channel matrix tend to 0. In addition, the sparse property is more obvious for LOS environments in Fig. 5(b) than that for NLOS environments in Fig. 5(d).

Fig. 6(a) and (b) illustrate the absolute values of the SCCF and ACCF, respectively. With the increase of antenna spacing in Fig. 6(a) and beam spacing in Fig. 6(b), the absolute values of the

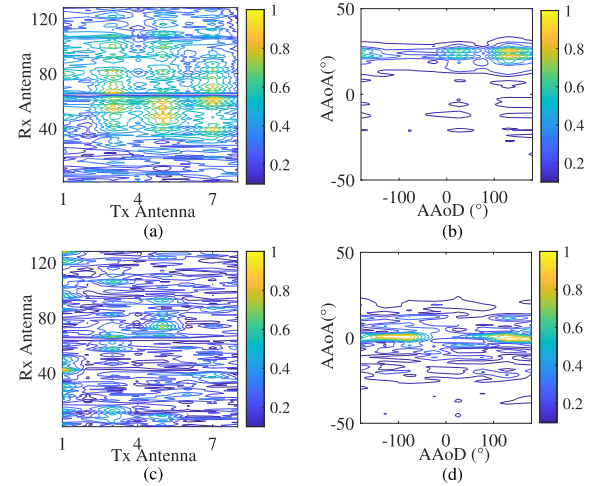


Fig. 5. Normalized channel matrices in LOS environments (Route 1, Position 7) in the (a) array and (b) angle domains and in NLOS environments (Route 1, Position 3) in the (c) array and (d) angle domains.

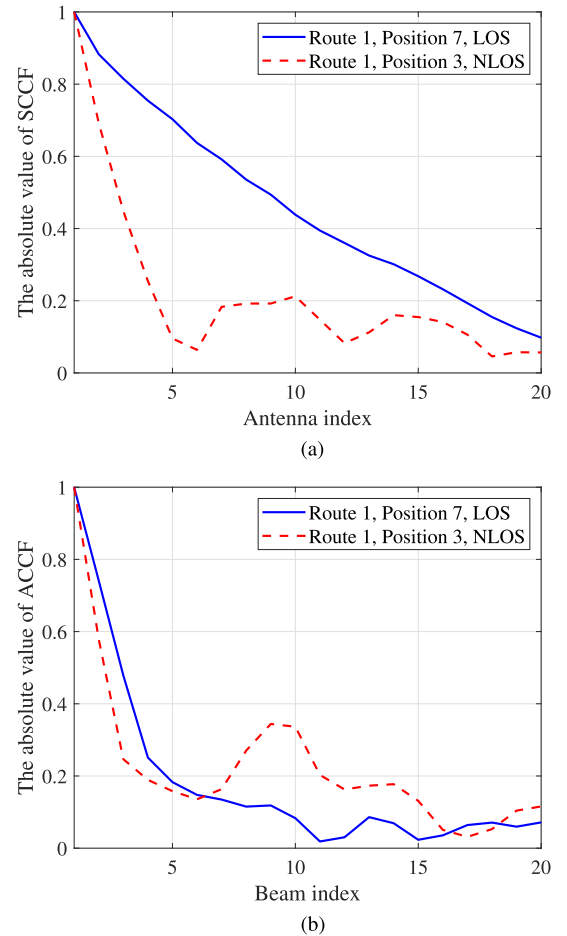


Fig. 6. The absolute values of the (a) SCCF and (b) ACCF.

SCCF and ACCF become smaller, respectively. By comparing the antenna correlations in LOS and NLOS environments in Fig. 6(a), we find that the correlation is larger in LOS environments than that in NLOS environments in the array domain. However, the correlations are smaller in both LOS and NLOS

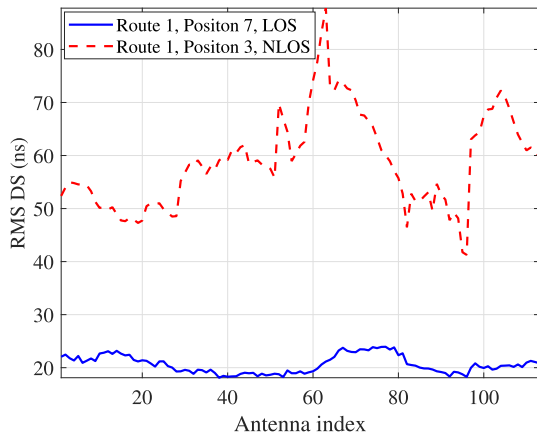


Fig. 7. The RMS DS along antenna array.

environments for the angle domain in Fig. 6(b) than those for the array domain in Fig. 6(a).

Fig. 7 illustrates the RMS DS along antenna array in LOS and NLOS environments. Note that the size of a sliding window is 16 antennas for SAGE algorithm. The RMS DS in NLOS environments is larger than that in LOS environments, which shows that the shadowing from trees, cars, and pedestrians increases the RMS DS. Furthermore, the variation of RMS DS along antenna array shows spatial non-stationarity of the ultra-massive MIMO antenna array.

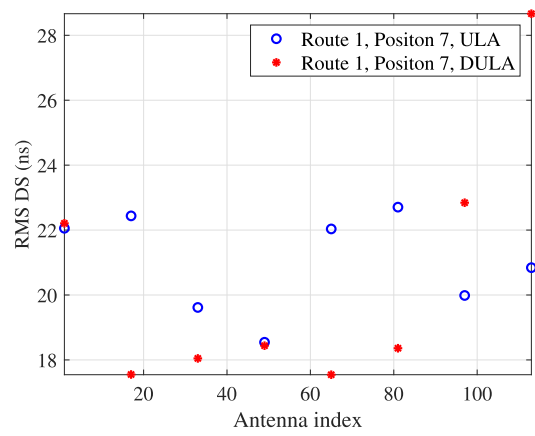
Fig. 8(a) and (b) show the RMS DS and RMS AS along the ULA and DULA with a sliding window size of 16 antennas in LOS environments, respectively. Comparing the ULA with the DULA, we find that the range of variation of RMS DS and AS for the DULA is larger than that for the ULA. This indicates that the longer antenna array experiences increased spatial non-stationarity.

Fig. 9 illustrates the FCFs of the array domain and angle domain of main beam in LOS and NLOS environments. Here, the main beam refers to the beam with the strongest power path. For the main beam, the absolute value of the FCF reaches the maximum. With the increase of frequency separation, the FCFs show decreasing trends. In addition, the FCF is larger in LOS environments than that in NLOS environments. This indicates a larger coherence bandwidth in LOS environments than that in NLOS environments of the array domain and angle domain of the main beam.

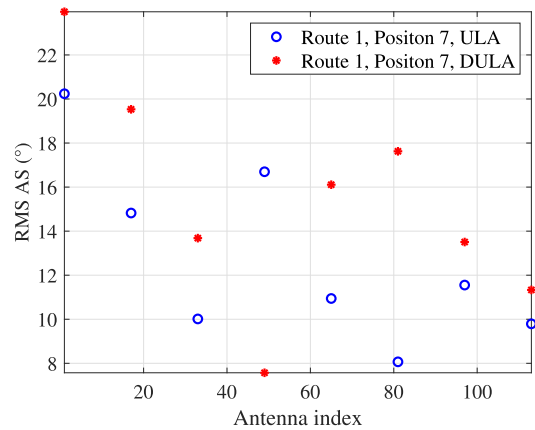
2) *Spherical Wavefront Property*: The spherical wavefront property can be reflected by the angle drift of LOS path along antenna array. Fig. 10 illustrates the AAoA of LOS path along antenna array. Compared with the ULA, the range of variation of AAoA for the DULA is larger, which indicates that the longer antenna array experiences a more obvious spherical wavefront, as might be expected.

B. Multi-User F2F Results and Analysis

1) *Non-Stationarity and Channel Hardening Property*: As illustrated in Fig. 11, the SVS along antenna array with a sliding window size of 32 antennas is larger in LOS environments than



(a)



(b)

Fig. 8. The variations of the (a) RMS DS and (b) RMS AS along antenna array.

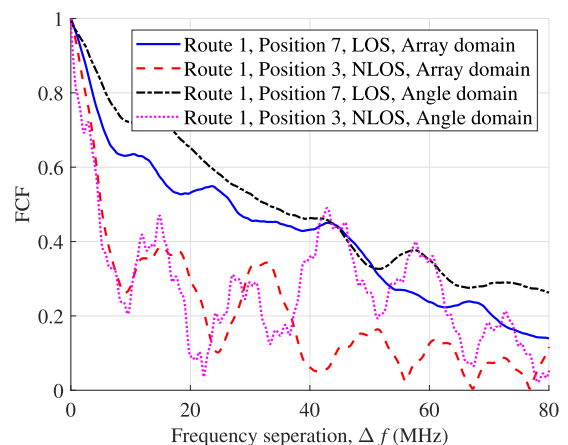


Fig. 9. The FCFs in LOS and NLOS environments.

that in NLOS environments, which indicates that the correlation between users is larger in LOS environments than that in NLOS environments. In addition, the variation of the SVS along antenna array illustrates spatial non-stationarity.

As illustrated in Fig. 12, the SPs are compared when the Rx is equipped with the ULA or DULA. Note that the distance between users is $D_{\text{user}} = 0.2$ m. The SP is larger in the ULA configuration than that in the DULA configuration at the Rx side,

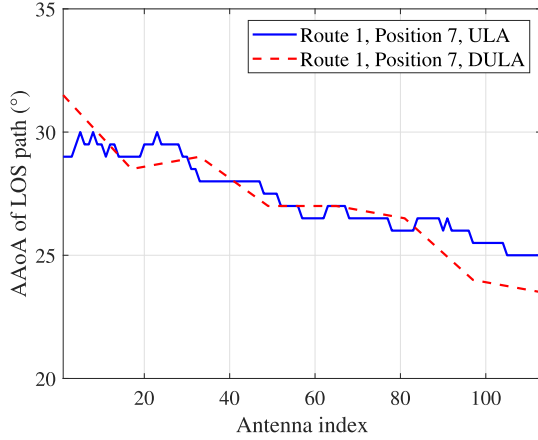


Fig. 10. The AAoA of LOS path along antenna array.

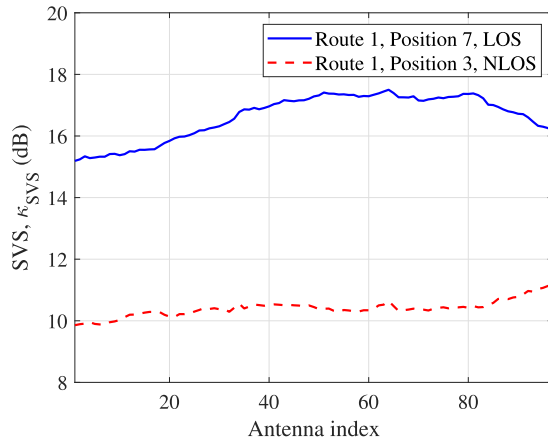


Fig. 11. The variation of the SVS along antenna array.

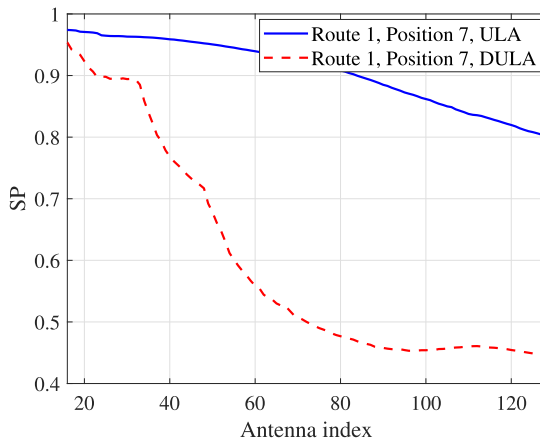


Fig. 12. The variation of the SP with the increase of Rx antenna numbers ($D_{\text{user}} = 0.2$ m).

which indicates that the longer antenna array can decrease the correlation between users and contribute to channel hardening property. Here, the channel hardening property, also known as favorable propagation condition, means that the channels for different users tend to be uncorrelated when using massive antennas at the BS side [18], [21], [26]. Additionally, the SP decreases with the increase of antennas at the BS side, which

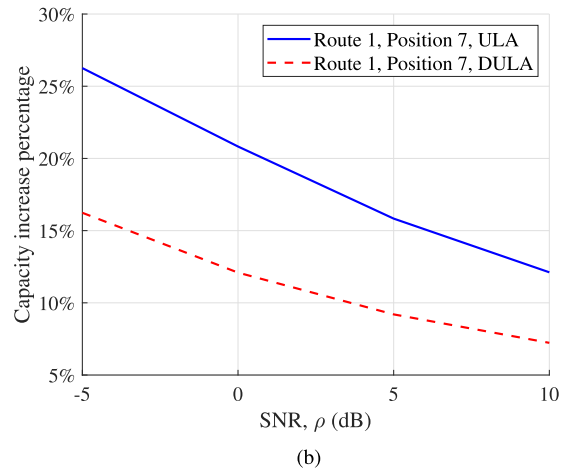
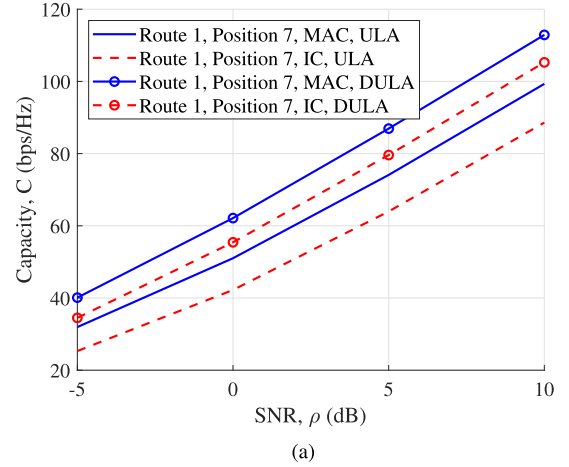


Fig. 13. The (a) MAC and IC capacities and (b) capacity increase percentage for the MAC capacity compared to the IC capacity ($D_{\text{user}} = 0.2$ m).

shows that more BS antennas can reduce the correlation between users.

2) *Multi-User Channel Capacity*: As illustrated in Fig. 13(a), the MAC and IC capacities of the ULA and DULA in LOS environments are investigated. The channel capacity of the DULA is larger than that of the ULA for both the MAC capacity and the IC capacity. This indicates that longer antenna array can increase channel capacity in LOS environments. In addition, for the same Rx antenna array configuration, the MAC capacity is larger than IC capacity and the percentage of improvement is shown in Fig. 13(b). We can see that the percentage of improvement for the MAC capacity compared to the IC capacity decreases with the increase of SNRs for both the ULA and DULA configurations. In addition, the percentage of improvement for the DULA is smaller compared to that for the ULA.

C. Single-User F2M Results and Analysis

1) *Non-Stationarity and Sparse Property*: The LCR refers to how often the envelope crosses a reference level in the positive or negative going direction. The AFD refers to the average time duration the envelope remains below a reference level [44].

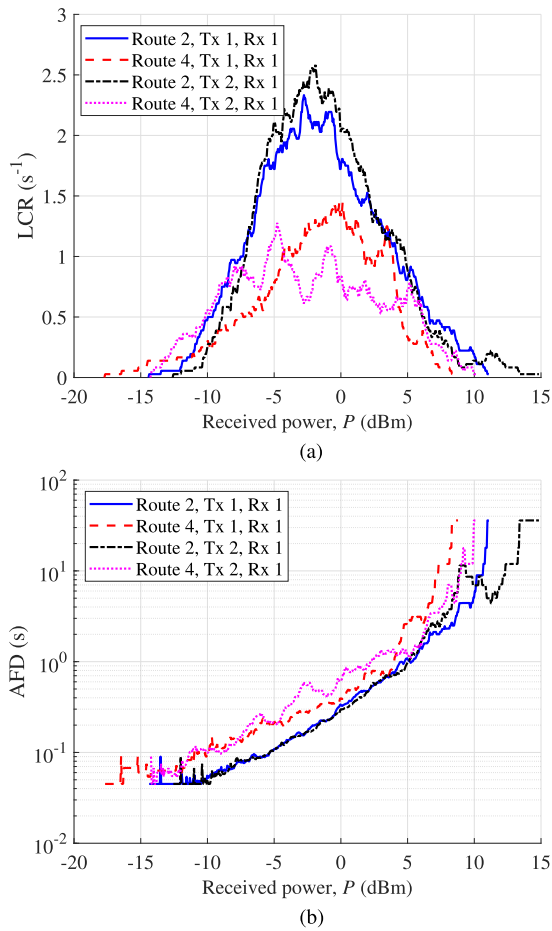


Fig. 14. The (a) LCR and (b) corresponding AFD of the received power.

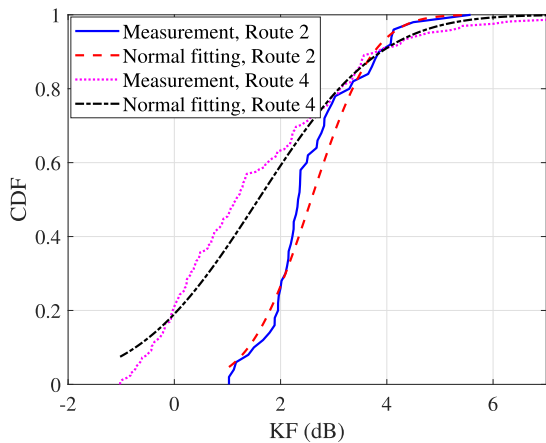


Fig. 15. CDFs of the KF for Route 2 and Route 4.

Fig. 14(a) and (b) show the LCR and AFD of the received power in the case of different Tx antennas and the same Rx antenna for Route 2 and Route 4. From the variations of the LCR and AFD, we can find that the choice of the reference level has a lot of influence on the LCR and AFD. The LCR is larger and the AFD is smaller for Route 2 than those for Route 4 when the reference level is in the range of -10 dB to 10 dB.

The KF can be calculated by moment method in [45]. Fig. 15 shows the cumulative distribution functions (CDFs) of the KF for

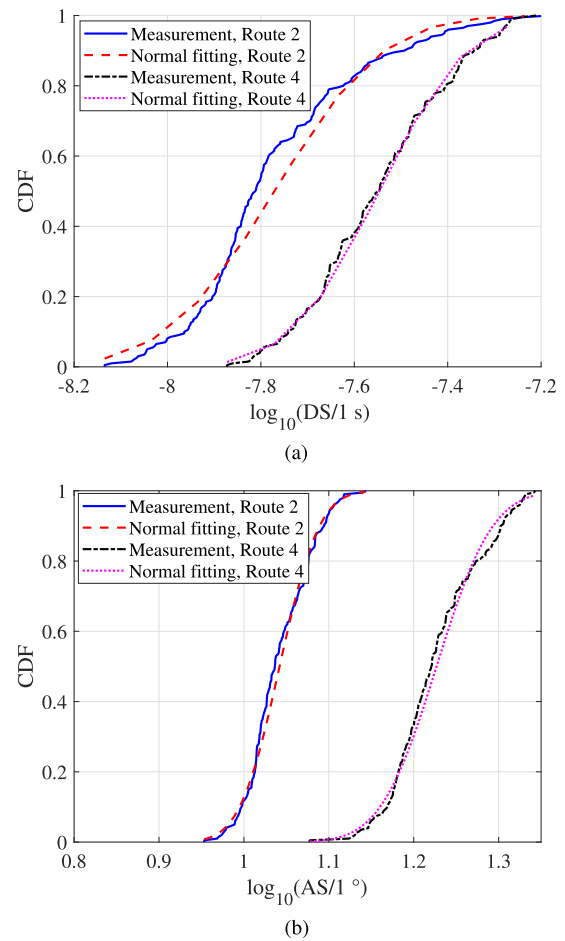


Fig. 16. CDFs of the (a) RMS DS and (b) RMS AS for Route 2 and Route 4.

Route 2 and Route 4, which can be fitted by normal distribution with $N(2.58, 0.92^2)$ and $N(1.58, 1.8^2)$, respectively. The KF for Route 2 is larger than that for Route 4, which indicates that the trees, cars, and pedestrians decrease the KF for Route 4. Note that the KF is an important large scale parameter (LSP) and its distribution can be used in future channel models and give guidance for the parameter setting.

Fig. 16(a) shows the CDFs of RMS DS for Route 2 and Route 4, which can be fitted by a base 10 lognormal distribution with $N(-7.46, 0.19^2)$ and $N(-7.31, 0.20^2)$, respectively. The lognormal distribution refers to that the CDF of DS is obtained by calculating $\log_{10}(DS/1 \text{ s})$. Fig. 16(b) shows the CDFs of RMS AS for Route 2 and Route 4, which can be fitted by a base 10 lognormal distribution with $N(1.1, 0.03^2)$ and $N(1.24, 0.05^2)$, respectively. The lognormal distribution refers to that the CDF of AS is obtained by computing $\log_{10}(AS/1^\circ)$. The RMS DS and RMS AS are larger for Route 4 than those for Route 2, which indicates that the trees, cars, and pedestrians increase the RMS DS and RMS AS for Route 4. Similarly, the RMS DS and RMS AS are important LSPs and their distributions can be used in future channel models as a reference for parameter settings.

The path number is the detected number of multipaths, which can be calculated by the same algorithm used in Fig. 4. As shown in Fig. 17, the CDFs of path numbers can be fitted by

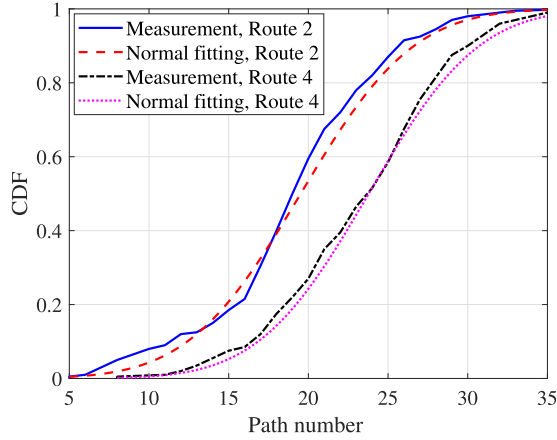


Fig. 17. CDFs of the path number for Route 2 and Route 4.

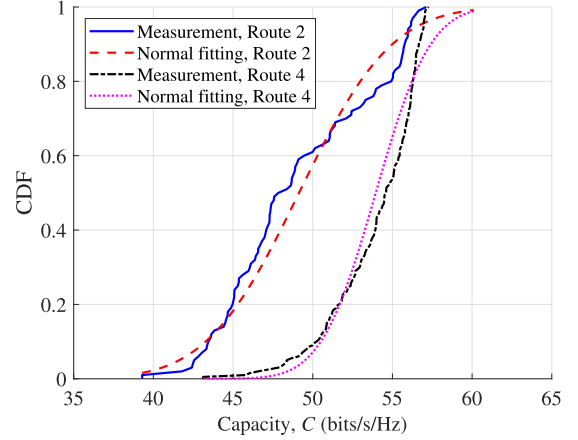


Fig. 19. CDFs of the channel capacity for Route 2 and Route 4.

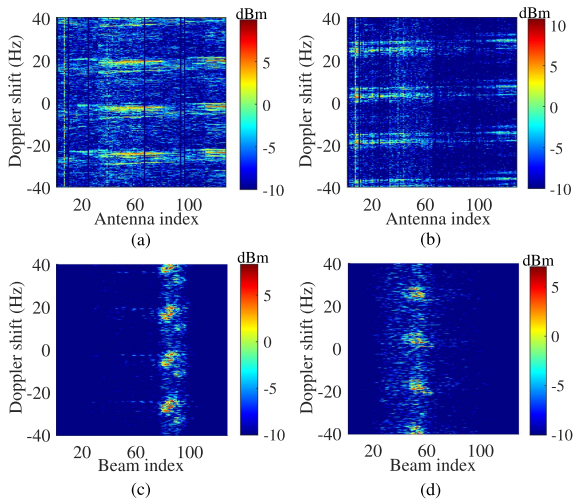


Fig. 18. The Doppler PSDs of the array domain for (a) Route 2 and (b) Route 4 and the angle domain for (c) Route 2 and (d) Route 4.

normal distribution with $N(19.52, 5.55^2)$ and $N(23.79, 5.42^2)$ for Route 2 and Route 4, respectively. The path number for Route 4 is larger than that for Route 2, which indicates that the trees, cars, and pedestrians increase the path number for Route 4. The distribution of path numbers can be used as a reference in future channel models.

Fig. 18(a) and (b) illustrate the Doppler PSDs at 5.3 GHz frequency point in the array domain. Fig. 18(c) and (d) illustrate the Doppler PSDs at 5.3 GHz frequency point in the angle domain. Compared with the array domain, the Doppler PSD appears more sparse in the angle domain.

2) *Single-User Channel Capacity*: As shown in Fig. 19, the CDFs of channel capacity can be fitted by normal distribution with $N(49.14, 4.57^2)$ and $N(53.95, 2.70^2)$ for Route 2 and Route 4, respectively. The channel capacity for Route 4 is larger than that for Route 2, which indicates that the trees, cars, and pedestrians increase the channel capacity for Route 4. Again, the channel capacity distribution can be used as a reference in future channel models.

For clarity, specific features of ultra-massive MIMO channels and corresponding statistical properties mentioned above are summarized in Table I.

TABLE I
SPECIFIC FEATURES OF ULTRA-MASSIVE MIMO CHANNELS AND
CORRESPONDING STATISTICAL PROPERTIES

Specific features	Statistical properties
Spatial non-stationarity	SCCF
Spherical wavefront property	AAoA of LOS path
Channel hardening property	SVS, SP
Sparse property in the angle domain	Normalized channel matrix in the angle domain, Doppler PSD

V. CONCLUSION

In this paper, 5.3 GHz band ultra-massive MIMO channel measurements with two antenna array configurations and in three scenarios have been conducted. The comprehensive statistical properties have been investigated, including the DPSD, SCCF, ACCF, RMS DS, FCF, RMS AS, AAoA of LOS path, SVS, SP, LCR, AFD, KF, path number, Doppler PSD, etc. The analysis of the DPSD illustrates that the detected number of multipaths in NLOS environments is larger than that in LOS environments. By the investigation of the SCCF and ACCF, we have found that the correlations are larger in LOS environments than those in NLOS environments in the array domain. However, the correlations are smaller for both LOS and NLOS environments in the angle domain than those in the array domain. The RMS DS along the antenna array in NLOS environments is larger than that in LOS environments, which shows that the shadowing from trees, cars, and pedestrians can increase the RMS DS. FCF results tell us that the coherence bandwidth in LOS environments is larger than that in NLOS environments. The variations of RMS DS, RMS AS, and the AAoA of LOS path along antenna array show that the longer antenna array makes the spatial non-stationarity and spherical wavefront properties more obvious. The variation of the SVS along antenna array shows that the correlation between users is larger in LOS environments than that in NLOS environments. SP results have illustrated that the longer antenna array can decrease the correlation between users in LOS environments. From the study of the multi-user MAC and IC capacities, we can see that channel capacities for the DULA are larger than those for the ULA in LOS environments. The KF, RMS DS, RMS AS, path number, and single-user channel

capacity for Route 2 and Route 4 follow normal or lognormal distributions. Larger LCR leads to a smaller AFD. In addition, the Doppler PSD appears more sparse in the angle domain than that in the array domain.

In the future, we will conduct ultra-massive MIMO channel measurements towards more frequency bands, scenarios, and antenna configurations. The similarity and difference of channel characteristics under different frequency bands and/or antenna configurations will be investigated. This will provide useful guidance for channel modeling, system design, and performance evaluation of 6G wireless communication systems.

REFERENCES

- [1] E. Björnson, J. Hoydis, and L. Sanguinetti, "Massive MIMO networks: Spectral, energy, and hardware efficiency," *Found. Trends Signal Process.*, vol. 11, no. 3, pp. 154–655, 2017.
- [2] E. G. Larsson, O. Edfors, F. Tufvesson, and T. L. Marzetta, "Massive MIMO for next generation wireless systems," *IEEE Commun. Mag.*, vol. 52, no. 2, pp. 186–195, Feb. 2014.
- [3] X.-H. You et al., "Towards 6G wireless communication networks: Vision, enabling technologies, and new paradigm shifts," *Sci. China Inf. Sci.*, vol. 64, no. 1, Jan. 2021, Art. no. 110301, doi: [10.1007/s11432-020-2955-6](https://doi.org/10.1007/s11432-020-2955-6).
- [4] C.-X. Wang et al., "On the road to 6G: Visions, requirements, key technologies and testbeds," *IEEE Commun. Surv. Tut.*, vol. 25, no. 2, pp. 905–974, Second quarter 2023.
- [5] Y. Yuan et al., "A 3D geometry-based THz channel model for 6G ultra massive MIMO systems," *IEEE Trans. Veh. Technol.*, vol. 71, no. 3, pp. 2251–2266, Mar. 2022.
- [6] M. Shafi et al., "5G: A tutorial overview of standards, trials, challenges, deployment, and practice," *IEEE J. Sel. Areas Commun.*, vol. 35, no. 6, pp. 1201–1221, Jun. 2017.
- [7] J. Wang, C.-X. Wang, J. Huang, H. Wang, X. Q. Gao, and Y. Hao, "A novel 3D non-stationary GBSM for 6G THz ultra-massive MIMO wireless systems," *IEEE Trans. Veh. Technol.*, vol. 70, no. 12, pp. 12312–12324, Dec. 2021.
- [8] W. Li, L. Liu, C. Tao, Y. Lu, J. Xiao, and P. Liu, "Channel measurements and angle estimation for massive MIMO systems in a stadium," in *Proc. 17th Int. Conf. Adv. Commun. Technol.*, 2015, pp. 105–108.
- [9] Y. Lu, C. Tao, and L. Liu, "Research on propagation characteristics of massive MIMO channel at 1.4725 GHz," in *Proc. IEEE 85th Veh. Technol. Conf.*, 2017, pp. 1–5.
- [10] S. Wu, C.-X. Wang, e. H. M. Aggoune, M. M. Alwakeel, and X.-H. You, "A general 3D non-stationary 5G wireless channel model," *IEEE Trans. Commun.*, vol. 66, no. 7, pp. 3065–3078, Jul. 2018.
- [11] C. F. López and C.-X. Wang, "Novel 3D non-stationary wideband models for massive MIMO channels," *IEEE Trans. Wireless Commun.*, vol. 17, no. 5, pp. 2893–2905, May 2018.
- [12] C.-X. Wang, J. Bian, J. Sun, W. Zhang, and M. Zhang, "A survey of 5G channel measurements and models," *IEEE Commun. Surv. Tut.*, vol. 20, no. 4, pp. 3142–3168, Fourthquarter 2018.
- [13] C. F. López, C.-X. Wang, and Y. Zheng, "A 3D non-stationary wideband massive MIMO channel model based on ray-level evolution," *IEEE Trans. Commun.*, vol. 70, no. 1, pp. 621–634, Jan. 2022.
- [14] X. Gao, O. Edfors, F. Rusek, and F. Tufvesson, "Massive MIMO performance evaluation based on measured propagation data," *IEEE Trans. Wireless Commun.*, vol. 14, no. 7, pp. 3899–3911, Jul. 2015.
- [15] X. Gao, F. Tufvesson, O. Edfors, and F. Rusek, "Measured propagation characteristics for very-large MIMO at 2.6 GHz," in *Proc. Conf. Rec. 46th Asilomar Conf. Signals, Syst. Comput.*, 2012, pp. 295–299.
- [16] S. Payami and F. Tufvesson, "Channel measurements and analysis for very large array systems at 2.6 GHz," in *Proc. 6th Eur. Conf. Antennas Propag.*, 2012, pp. 433–437.
- [17] S. Payami and F. Tufvesson, "Delay spread properties in a measured massive MIMO system at 2.6 GHz," in *Proc. IEEE 24th Annu. Int. Symp. Pers., Indoor, Mobile Radio Commun.*, 2013, pp. 53–57.
- [18] P. Zhang, J. Chen, X. Yang, N. Ma, and Z. Zhang, "Recent research on massive MIMO propagation channels: A survey," *IEEE Commun. Mag.*, vol. 56, no. 12, pp. 22–29, Dec. 2018.
- [19] J. Xi, J. Zhang, L. Tian, and Y. Wu, "Capacity analysis based on channel measurements of massive MU-MIMO system at 3.5 GHz," in *Proc. IEEE Int. Conf. Comput. Commun.*, 2017, pp. 79–83.
- [20] H. Q. Ngo, E. G. Larsson, and T. L. Marzetta, "Aspects of favorable propagation in massive MIMO," in *Proc. IEEE 22nd Eur. Signal Process. Conf.*, 2014, pp. 76–80.
- [21] J. Chen, "When does asymptotic orthogonality exist for very large arrays," in *Proc. IEEE Glob. Commun. Conf.*, 2013, pp. 4146–4150.
- [22] S. Sangodoyin et al., "Cluster characterization of 3-D MIMO propagation channel in an urban macrocellular environment," *IEEE Trans. Wireless Commun.*, vol. 17, no. 8, pp. 5076–5091, Aug. 2018.
- [23] J. Zhang, Z. Zheng, Y. Zhang, J. Xi, X. Zhao, and G. Gui, "3D MIMO for 5G NR: Several observations from 32 to massive 256 antennas based on channel measurement," *IEEE Commun. Mag.*, vol. 56, no. 3, pp. 62–70, Mar. 2018.
- [24] Á. O. Martínez, E. D. Carvalho, and J. Ø. Nielsen, "Massive MIMO properties based on measured channels: Channel hardening, user decorrelation and channel sparsity," in *Proc. IEEE 50th Asilomar Conf. Signals, Syst. Comput.*, 2016, pp. 1804–1808.
- [25] Á. O. Martínez, J. Ø. Nielsen, E. D. Carvalho, and P. Popovski, "An experimental study of massive MIMO properties in 5G scenarios," *IEEE Trans. Antennas Propag.*, vol. 66, no. 12, pp. 7206–7215, Dec. 2018.
- [26] Y. Zheng et al., "Ultra-massive MIMO channel measurements at 5.3 GHz and a general 6G channel model," *IEEE Trans. Veh. Technol.*, vol. 72, no. 1, pp. 20–34, Jan. 2023.
- [27] A. M. Sayeed, "Deconstructing multiantenna fading channels," *IEEE Trans. Signal Process.*, vol. 50, no. 10, pp. 2563–2579, Oct. 2002.
- [28] K. I. Pedersen, B. H. Fleury, and P. E. Mogensen, "High resolution of electromagnetic waves in time-varying radio channels," in *Proc. IEEE 8th Int. Symp. Pers., Indoor Mobile Radio Commun.*, 1997, pp. 650–654.
- [29] J. Huang, C.-X. Wang, R. Feng, J. Sun, W. Zhang, and Y. Yang, "Multi-frequency mmWave massive MIMO channel measurements and characterization for 5G wireless communication systems," *IEEE J. Sel. Areas Commun.*, vol. 35, no. 7, pp. 1591–1605, Jul. 2017.
- [30] X. Yin, L. Ouyang, and H. Wang, "Performance comparison of SAGE and MUSIC for channel estimation in direction-scan measurements," *IEEE Access*, vol. 4, pp. 1163–1174, 2016.
- [31] C. Sun, X. Q. Gao, S. Jin, M. Matthaiou, Z. Ding, and C. Xiao, "Beam division multiple access transmission for massive MIMO communications," *IEEE Trans. Commun.*, vol. 63, no. 6, pp. 2170–2184, Jun. 2015.
- [32] J. Bian et al., "A novel 3D beam domain channel model for massive MIMO communication systems," *IEEE Trans. Commun.*, vol. 22, no. 3, pp. 1618–1632, Mar. 2023.
- [33] X. Cai et al., "An empirical air-to-ground channel model based on passive measurements in LTE," *IEEE Trans. Veh. Technol.*, vol. 68, no. 2, pp. 1140–1154, Feb. 2019.
- [34] K. Guan et al., "Channel characterization for intra-wagon communication at 60 and 300 GHz bands," *IEEE Trans. Veh. Technol.*, vol. 68, no. 6, pp. 5193–5207, Jun. 2019.
- [35] X. Cai, B. Peng, X. Yin, and A. P. Yuste, "Hough-transform-based cluster identification and modeling for V2V channels based on measurements," *IEEE Trans. Veh. Technol.*, vol. 67, no. 5, pp. 3838–3852, May 2018.
- [36] Z. Ma et al., "Impact of UAV rotation on MIMO channel characterization for air-to-ground communication systems," *IEEE Trans. Veh. Technol.*, vol. 69, no. 11, pp. 12418–12431, Nov. 2020.
- [37] C.-X. Wang, Z. Lv, X. Q. Gao, X.-H. You, Y. Hao, and H. Haas, "Pervasive channel modeling theory and applications to 6G GBSMs for all frequency bands and all scenarios," *IEEE Trans. Veh. Technol.*, vol. 71, no. 9, pp. 9159–9173, Sep. 2022.
- [38] Y. He et al., "A novel 3D non-stationary maritime wireless channel model," *IEEE Trans. Commun.*, vol. 70, no. 3, pp. 2102–2116, Mar. 2022.
- [39] J. Bian, C.-X. Wang, X. Q. Gao, X.-H. You, and M. Zhang, "A general 3D non-stationary wireless channel model for 5G and beyond," *IEEE Trans. Wireless Commun.*, vol. 20, no. 5, pp. 3211–3224, May 2021.
- [40] D. Tse and P. Viswanath, *Fundamentals of Wireless Communication*, 1st ed. Cambridge, U.K.: Cambridge: Univ. Press, 2005.
- [41] J. Zhang, Y. Zhang, Y. Yu, R. Xu, Q. Zheng, and P. Zhang, "3-D MIMO: How much does it meet our expectations observed from channel measurements?," *IEEE J. Sel. Areas Commun.*, vol. 35, no. 8, pp. 1887–1903, Aug. 2017.
- [42] J. Huang, C.-X. Wang, Y. Yang, Y. Liu, J. Sun, and W. Zhang, "Channel measurements and modeling for 400–600-MHz bands in urban and suburban scenarios," *IEEE Int. Things J.*, vol. 8, no. 7, pp. 5531–5543, Apr. 2021.

- [43] J. Huang, C.-X. Wang, H. Chang, J. Sun, and X. Q. Gao, "Multi-frequency multi-scenario millimeter wave MIMO channel measurements and modeling for 5G wireless communication systems," *IEEE J. Sel. Areas Commun.*, vol. 38, no. 9, pp. 2010–2025, Sep. 2020.
- [44] J. Bian et al., "A WINNER based 3-D non-stationary wideband MIMO channel model," *IEEE Trans. Wireless Commun.*, vol. 17, no. 3, pp. 1755–1767, Mar. 2018.
- [45] L. Hao, J. Rodríguez-Piñero, X. Yin, and H. Wang, "Measurement-based massive MIMO polarimetric channel characterization in outdoor environment," *IEEE Access*, vol. 7, pp. 171285–171296, 2019.



Yi Zheng received the B.Sc. degree from Dalian Maritime University, Dalian, China, in 2016, and the M.Eng. degree in 2019 from Southeast University, Nanjing, China, where she is currently working toward the Ph.D. degree with the National Mobile Communications Research Laboratory. Her research interests include massive MIMO channel measurements and modeling and holographic MIMO channel characterization and modeling.



Cheng-Xiang Wang (Fellow, IEEE) received the B.Sc. and M.Eng. degrees in communication and information systems from Shandong University, Jinan, China, in 1997 and 2000, respectively, and the Ph.D. degree in wireless communications from Aalborg University, Aalborg, Denmark, in 2004.

He was a Research Assistant with the Hamburg University of Technology, Hamburg, Germany, from 2000 to 2001, a Visiting Researcher with Siemens AG Mobile Phones, Munich, Germany, in 2004, and a Research Fellow with the University of Agder, Grimstad, Norway, from 2001 to 2005. Since 2005, he has been with Heriot-Watt University, Edinburgh, U.K., where he was promoted to a Professor in 2011. In 2018, he joined Southeast University, Nanjing, China, as a Professor. He is also a part-time Professor with Purple Mountain Laboratories, Nanjing, China. He has authored four books, three book chapters, and more than 490 papers in refereed journals and conference proceedings, including 27 highly cited papers. He has also delivered 24 invited keynote speeches/talks and 15 tutorials in international conferences. His research interests include wireless channel measurements and modeling, 6G wireless communication networks, and electromagnetic information theory.

Dr. Wang is a Member of the European Academy of Sciences and Arts (EASA), a Fellow of the Royal Society of Edinburgh (FRSE), IEEE, IET, and China Institute of Communication (CIC), an IEEE Communications Society Distinguished Lecturer in 2019 and 2020, a Highly-Cited Researcher recognized by Clarivate Analytics in 2017–2020, and one of the most cited Chinese Researchers recognized by Elsevier in 2021. He is currently an Executive Editorial Committee Member of the IEEE TRANSACTIONS ON WIRELESS COMMUNICATIONS. He was the Editor of more than ten international journals, including the IEEE TRANSACTIONS ON WIRELESS COMMUNICATIONS from 2007 to 2009, IEEE TRANSACTIONS ON VEHICULAR TECHNOLOGY from 2011 to 2017, and IEEE TRANSACTIONS ON COMMUNICATIONS from 2015 to 2017. He was the Guest Editor of the IEEE JOURNAL ON SELECTED AREAS IN COMMUNICATIONS, Special Issue on Vehicular Communications and Networks (Lead Guest Editor), Special Issue on Spectrum and Energy Efficient Design of Wireless Communication Networks, and Special Issue on Airborne Communication Networks. He was also the Guest Editor of the IEEE TRANSACTIONS ON BIG DATA, Special Issue on Wireless Big Data, and IEEE TRANSACTIONS ON COGNITIVE COMMUNICATIONS AND NETWORKING, Special Issue on Intelligent Resource Management for 5G and Beyond. He was a TPC Member, the TPC Chair, and General Chair of more than 80 international conferences. He was the recipient of 15 Best Paper Awards from IEEE GLOBECOM 2010, IEEE ICCT 2011, ITST 2012, IEEE VTC-Spring 2013, IWCMC 2015, IWCMC 2016, IEEE/CIC ICC 2016, WPMC 2016, WOCC 2019, IWCMC 2020, WCSP 2020, CSPS 2021, WCSP 2021, and IEEE/CIC ICC 2022.



Jie Huang (Member, IEEE) received the B.E. degree in information engineering from Xidian University, Xi'an, China, in 2013, and the Ph.D. degree in information and communication engineering from Shandong University, Jinan, China, in 2018. From October 2018 to October 2020, he was a Postdoctoral Research Associate with National Mobile Communications Research Laboratory, Southeast University, supported by the National Postdoctoral Program for Innovative Talents. From January 2019 to February 2020, he was a Postdoctoral Research Associate with Durham University, Durham, U.K. Since March 2019, he has been a part-time Researcher with Purple Mountain Laboratories, China. Since November 2020, he has been an Associate Professor with the National Mobile Communications Research Laboratory, Southeast University, Nanjing, China. He has authored and coauthored more than 70 papers in refereed journals and conference proceedings. His research interests include millimeter wave, massive MIMO, reconfigurable intelligent surface channel measurements and modeling, wireless Big Data, and 6G wireless communications. He was the recipient of the Best Paper Awards from WPMC 2016, WCSP 2020, and WCSP 2021. He has delivered eight tutorials in IEEE/CIC ICC 2021, IEEE PIMRC 2021, IEEE ICC 2022, IEEE VTC-Spring 2022, IEEE/CIC ICC 2022, IEEE VTC-Fall 2022, IEEE PIMRC 2022, and IEEE Globecom 2022.



Rui Feng (Member, IEEE) received the B.Sc. degree in communication engineering and the M.Eng. degree in signal and information processing from Yantai University, Yantai, China, in 2011 and 2014, respectively, and the Ph.D. degree in communication and information system from Shandong University, Jinan, China, in 2018. From July 2018 to September 2020, she was a Lecture with Ludong University, Yantai, China. She is currently a Postdoctoral Research Associate of Purple Mountain Laboratories and Southeast University, Nanjing, China. Her research interests include (ultra-) massive MIMO channel modeling theory and beam domain channel modeling.



John S. Thompson (Fellow, IEEE) received the Ph.D. degree in electrical engineering from the University of Edinburgh, Edinburgh, U.K., in 1995. He is currently the Personal Chair of signal processing and communications with the School of Engineering, University of Edinburgh, Edinburgh, U.K. He specializes in antenna array processing, energy-efficient wireless communications, and application of machine learning to wireless communications problems. He has authored or coauthored in excess of 400 papers on these topics. His work has been regularly cited by the wireless community and from 2015 to 2018, he was recognized by Thomson Reuters as a Highly Cited Researcher. He is currently the Area Editor handling wireless communications topics for the IEEE TRANSACTIONS ON GREEN COMMUNICATIONS AND NETWORKING. In January 2016, he was elevated to Fellow of the IEEE for Contributions to Antenna Arrays and Multihop Communications.